

Geometry Dependence of Magnetization Reversal in Nanocomposite Alloys

RALPH SKOMSKI,^{1,4} PRIYANKA MANCHANDA,¹ ICHIRO TAKEUCHI,² and JUN CUI³

1.—Department of Physics and Astronomy and Nebraska Center for Materials and Nanoscience, University of Nebraska, Lincoln, NE 68588, USA. 2.—Department of Materials Science and Engineering, University of Maryland, College Park, MD 20742, USA. 3.—Energy and Environment Directorate, Pacific Northwest National Laboratory, Richland, WA 99354, USA. 4.—e-mail: rskomski@neb.rr.com

The geometrical optimization of aligned hard-soft permanent-magnet nanocomposites is investigated by model calculations. Considered criteria are the shapes of the soft and *c*-axis-aligned hard phases, the packing fraction of the soft phase, and magnetostatic interactions. Taking into account that the energy product is enhanced via the volume fraction of the soft phase, subject to maintaining coercivity, we find that the best structures are soft-magnetic cubes as well as long rods with a square cross section. Comparing embedded soft cubes with embedded soft spheres of the same size, our nucleation-field analysis shows that the volume fraction of the soft phase is enhanced by 91%, with a coercivity reduction of only 25%. Magnetostatic interactions often but not always deteriorate the permanent-magnet performance, as exemplified by the example of MnBi:FeCo bilayers and multilayers.

INTRODUCTION

Today's high-performance permanent magnets are made from intermetallic alloys containing iron-series transition metals, typically Fe or Co, and heavy elements.^{1,2} The latter are necessary to provide spin-orbit coupling, which is a necessary condition for magnetic anisotropy and hysteresis.³ Examples are rare-earth permanent magnets, most notably Nd₂Fe₁₄B and SmCo₅, and *L1*₀-ordered alloys, such as CoPt and FePt. However, the heavy elements in these alloys are normally very expensive. CoPt is no longer used in substantial quantities, and FePt applications are limited to magnetic recording media,^{4,5} where the mass of the material is very small. The rare-earth prices play an important role because magnets for motors and other applications are often bulky and must be produced in large numbers.

Nonmetallic magnets, such as SrFe₁₂O₁₉, can be produced cheaply and in large amounts,³ but their saturation magnetization M_s is low, diluted by the large O²⁻ ions that occupy most of the volume. In more detail, the maximum energy product $(BH)_{\max}$, which describes a magnetic material's ability to create a permanent magnetic field in free space,

cannot be larger than $\mu_0 M_s^2/4$. Moreover, this upper limit can only be achieved if the magnet has a high uniaxial anisotropy constant K and exhibits a microstructure that supports coercivity,^{6,7} ideally $H_c > M_s/2$.³ A further raw-materials-related complication is that today's energy-product record holder, Nd₂Fe₁₄B, requires Dy additions to realize a high coercivity at operation temperatures above 100°C, for example in automotive applications. Dy is expensive even by rare-earth standards and is in short supply due to the global trade situation and competing applications, for example optical displays and top-end light sources.

There are two basic strategies to solve this dilemma. First, there is ongoing research toward new intermetallic alloys with good permanent-magnet properties.⁸⁻¹¹ It focuses on light and heavy elements such as Mn and Bi, respectively, which are less expensive than their present-day counterparts. This is a challenge because these alloys must simultaneously exhibit a high saturation magnetization M_s , a high Curie temperature T_c , and a high anisotropy K .³

The second approach is *c*-axis-aligned hard-soft nanocomposites where the soft phase improves the

hard-magnetic performance the main phase.^{12–15} The idea behind this counterintuitive approach is to sacrifice some excess anisotropy and coercivity while enhancing magnetization and energy product beyond that of the hard phase, up to slightly higher than 1000 kJ/m³¹³ or twice the value for Nd₂Fe₁₄B. While experimental proofs of principle exist,^{16,17} the well-known and demanding challenge remains to add a substantial amount of the soft phase to boost the magnetization while maintaining an appreciable coercivity. Aside from a meaningful choice of the hard and soft phases and from the control of important details, such as the grain boundary microstructure, this requires appropriate sizes and geometries of the hard and soft regions. It is well established that the soft-phase regions cannot be much larger than twice the Bloch wall width $\delta_h = \pi (A/K_h)^{1/2}$ of the hard phase,^{12,13} irrespective of dimensionality. Because δ_h is of the order of 5 nm for very hard materials, this yields a maximum feature size of 10 nm.

In their 1991 paper, Kneller and Hawig¹² considered layered hard-soft nanostructures, whose micromagnetic behavior was well understood at that time due to earlier papers by Goto et al.,¹⁸ Kronmüller,¹⁹ and Nieber and Kronmüller.²⁰ The geometrical optimization or “rational design” of three-dimensional hard-soft nanostructures was pioneered by Skomski²¹ and by Skomski and Coey.¹³ The calculation on spherical soft inclusions in a very hard matrix²¹ was followed by several articles on a variety of geometries and limits, such as embedded soft cylinders,^{11,22,23} embedded soft cubes,²⁴ disordered nanostructures,^{13,22,23} and interacting soft regions.^{22,23} This predominantly analytic research has shown, for example, that the interaction between soft inclusions leads to micromagnetic delocalization through the hard phase, as contrasted to percolation of the soft phase, and that free soft-magnetic surfaces are extremely harmful to the nucleation field. It complements analytical and numerical calculations by other groups, for example on granular nanocomposites²⁵ and core shell structures.²⁶ The geometrical optimization has attracted renewed attention due to the recent rare-earth supply bottlenecks.^{11,27}

The purpose of this article is twofold. First, we discuss the limit of soft inclusions in a very hard matrix, which yields a very transparent understanding of geometrical and volume-fraction effects. Second, we investigate magnetostatic corrections, which often deteriorate the performance of permanent magnets but are shown to provide an innovative pathway toward new technology in a specific example.

Geometrical Optimization

To obtain an optimized hard-soft nanostructure, it is important to maximize the volume fraction of the soft phase without having the soft regions too far

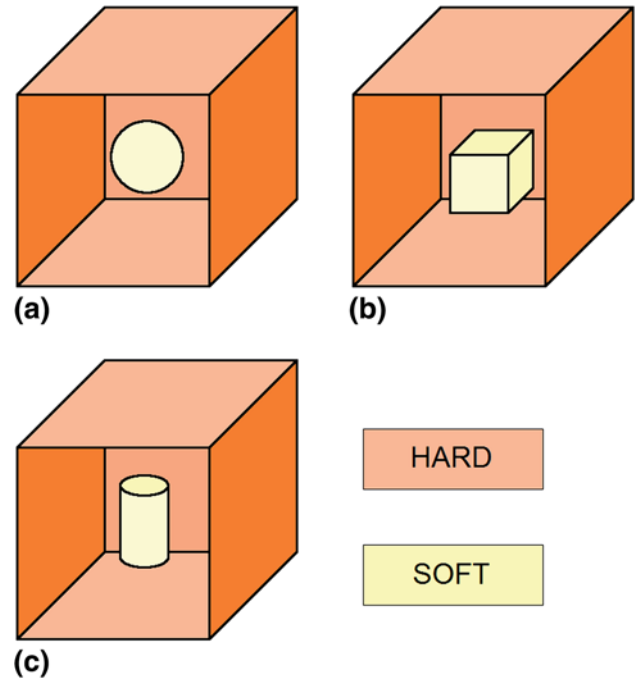


Fig. 1. Some hard-soft geometries. The aspect ratios $a:b:c$ (b) and $L:R$ (c) can be varied freely. In (c), the crystallographic c -axis of the hard phase is parallel to the cylinder axis.

away from the hard regions. Figure 1 shows some basic geometries considered in this context. If the volume fraction of the soft phase gets too big or if a soft region becomes too large, then the coercivity decreases and the energy product collapses.

The coercivity can be estimated by solving the nucleation-field equation

$$-A\nabla^2\phi + K_1(r)\phi + 1/2\mu_0M_sH\phi = 0 \quad (1)$$

subject to the appropriate boundary conditions.^{11,24} In this equation, A is the exchange stiffness, $K_1(r)$ is the local anisotropy constant ($K_1 = 0$ in the soft phase), M_s and H are the saturation magnetization, and $f(r)$ is the nucleation mode, or angle between magnetization and c -axis. Equation 1 has been solved for a number of geometries. In the hard-magnetic limit (large K_1), the solutions of this equation are the Bessel functions $J_\nu(x)$, so that

$$\phi(r) = r^{1-d/2}J_{d/2-1}(\kappa r) \quad (2)$$

By separation of variables, it is also possible to treat extruded geometries, such as cylinders of finite aspect ratios $\xi = L/2R$:

$$H_N = \frac{2A}{\mu_0M_sR^2} (c_2^2 + \pi^2/4\xi^2), \quad (3)$$

where $c_2 = 2.4048$ is the first zero of the “two-dimensional” Bessel function $J_0(\kappa r)$. For rectangular cuboids of dimensions a , b , and c , the same procedure yields

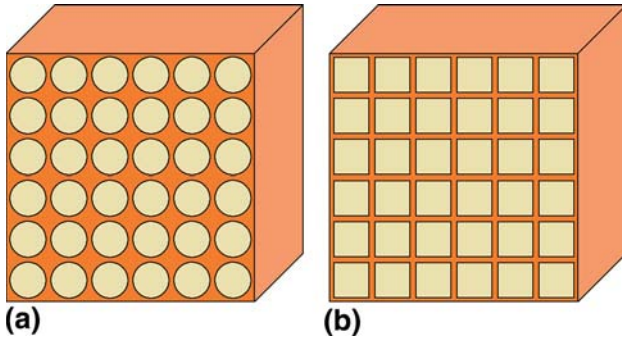


Fig. 2. Schematic hard-soft geometries: (a) embedded spheres and (b) embedded cubes.

$$H_N = \frac{2A}{\mu_0 M_s} (1/a^2 + 1/b^2 + 1/c^2) \quad (4)$$

This includes the well-known limits of thin films ($a = b = \infty, c = t$) and cubes ($a = b = c$).

Relative to the embedded spheres, this methods yield nucleation-field reductions by factors of 3/4 (embedded cubes), 1/2 (embedded wires with square cross section), and 1/4 (embedded layers).

To obtain an optimized hard-soft nanostructure, it is important to maximize the volume fraction of the soft phase without having soft regions too far away from the hard regions. A hard-phase thickness of 1–2 nm, essentially $(A/K_H)^{1/2}$, is already sufficient to create a substantial net exchange between the hard and soft phases, although this range increases if one uses “semihard” materials such as MnBi and MnAl as hard phases. Beyond this, there is no reason to have extended hard regions because they only slightly improve the coercivity but reduce the volume fraction f of the soft phase.

Figure 2 shows the outcome of this sandbox game. Compared with multilayers and embedded soft spheres (Fig. 2a), embedded soft cubes (Fig. 2b) are most promising because they waste less “dead” hard-magnetic volume distant from the soft phase. A straightforward comparison of the volumes of cubes and spheres yields a volume-fraction factor $6/\pi = 1.91$ in favor of the embedded cubes. In this configuration, the least amount of hard phase is wasted by occupying “dead” volume distant from the soft phase. On the downside, the coercivity of cubic inclusions is somewhat reduced compared with spherical inclusions, by 25% according to the analysis below Eq. 4. Similar considerations apply to the comparison of embedded long rods with square and circular cross sections (f increases by factor $4/\pi = 1.273$, whereas H_N decreases by a factor of $\pi^2/2c_2^2 = 0.852$). Note that the volume fraction is more important from a theoretical viewpoint, whereas coercivity is the main practical consideration.

Of course, the nucleation-field analysis of this section ignores domain-wall pinning, which may enhance the coercivity, $H_c > H_N$. On the other hand, it is extremely difficult to produce structures

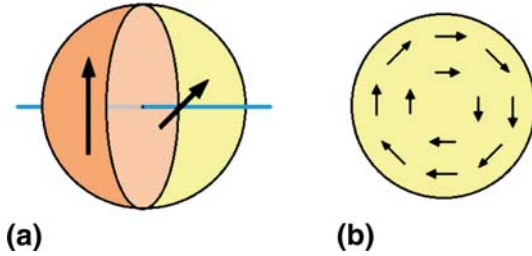


Fig. 3. Magnetostatic interactions: (a) two-spin model and (b) curling.

such as those shown in Fig. 2. The corresponding imperfections generally act as nucleation centers and *reduce* nucleation field and coercivity. In a slightly different context, this real-structure dependence of the coercivity is known as Brown’s paradox.⁶ The paradox is not a failure of theory or a sign of ivory-tower mentality, as sometimes assumed, but it is an indicator of our limited knowledge about real structure defects in a given material.⁶ An intriguing point is that the soft regions in Figs. 1 and 2 are also nucleation centers, meaning that these soft regions are both a part of Brown’s paradox itself and a part of its solution.

Interestingly, Eq. 1 does not support a “percolation” of the soft phase: The only geometrical consideration is the maximum distance of the soft phase from the hard phase. The difference between percolation and hard-soft nanostructuring can be seen, for example, by considering hard-soft multilayers with small periodicities, where the soft phase percolates without causing exchange decoupling.

Magnetostatic Effects

Equations 1–4 are exactly within the limit of very fine-grained hard magnets ($K_1 \gg \mu_0 M_s^2/4$). This is only approximately the case in practice, and numerical simulations²⁵ yield corrections that are sometimes substantial. Pinning effects and Brown’s paradox are not the only reasons for these corrections because magnetostatic effects are only very crudely included in Eq. 1, namely in form of effective anisotropy and effective interaction fields.²⁴ Here, we consider magnetostatic corrections from a fundamental viewpoint, with the aims of tracing harmful effects and identifying potential benefits.

An instructive example is the simple two-spin model of Fig. 3a, which has only two magnetic degrees of freedom, namely two rotation angles about a common axis.³ This model, which provides some qualitative and semiquantitative insight into hard-soft exchange coupling and magnetostatic interactions,²⁸ has recently been sophisticated by Lyubina et al.²⁹ to fully include nonlinear effects. Concerning magnetostatic interactions, the model favors antiparallel ($\uparrow\downarrow$) spin configurations. This is in close analogy to the behavior of two compass needles located side by side but modified by

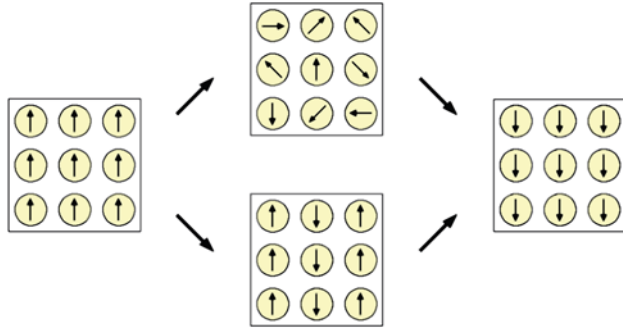


Fig. 4. Schematic spin structure during magnetization reversal. The two configurations in the middle have roughly the same magnetization but a drastically different spin structure.

exchange, which tries to keep the spins parallel, and magnetocrystalline anisotropy (K).

Magnetostatic interactions are often approximated by interaction fields ($H > H_{\text{eff}}$) and/or shape anisotropy ($K > K_{\text{eff}}$). However, Fig. 3b shows a curling or vortex state,³⁰ which cannot be described by these effective parameters. Such micromagnetic configurations are common and have a profound effect on hysteresis and energy product. Figure 4 illustrates the situation for an ensemble of interacting small particles. During magnetization reversal, the net magnetization M changes from positive (\uparrow) to negative (\downarrow), but depending on the strength of the interaction, the intermediate states at $M \sim 0$ may be disordered (top) or magnetostatically ordered (bottom). Such ordered magnetization configurations have the character of columnar structures or, more generally, *interaction domains*.^{31–33} Another interaction effect is hysteresis-loop overskewing, where the interaction between particles causes a cooperative or “avalanche-like” magnetization reversal.^{24,34} For example, ferromagnetic interatomic exchange fields in compressed metallic powders tend to exceed 100 T, but the observed coercivities do not exceed values of the order of 1 T.

From a broad perspective, interaction effects become important if they are able to compete with magnetic inhomogeneities.²⁴ For example, individual particles may have different c -axis orientations, as in the top part of Fig. 4, or they may be magnetically nonequivalent for metallurgical reasons due to surface morphology or, in the case of FePt, different degrees of $L1_0$ order. To investigate how the hysteresis loops are affected by interactions, we first consider interaction-free particle ensembles. The simplest hysteresis model is the Preisach model,³⁵ which assumes that each particle has two magnetization states only, namely \uparrow and \downarrow . This model is highly simplistic and fails to describe most scenarios encountered in magnetism,³⁶ but it works reasonably well for ensembles of c -axis-aligned small particles. In the Preisach model, each particle is characterized by an individual switching field

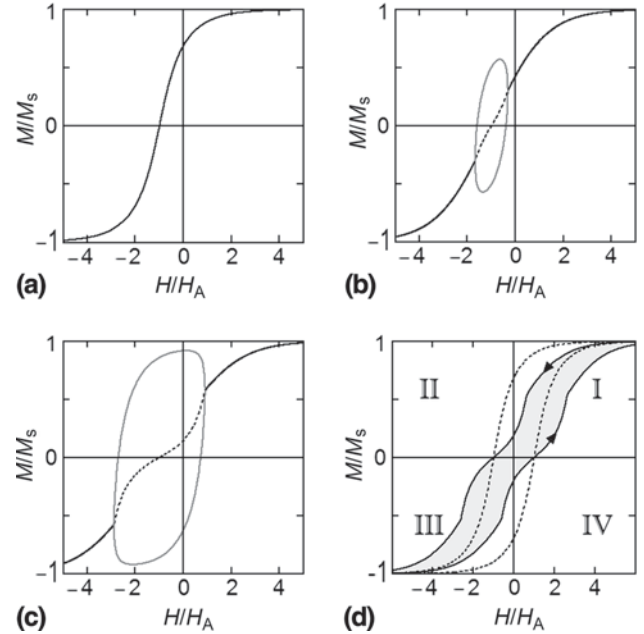


Fig. 5. Formation of columnar spin structures: (a) noninteracting case, (b) moderate magnetostatic interaction, (c) strong magnetostatic interactions, and (d) hysteresis-loop shape for strong interactions. For clarity, only the descending hysteresis-loop branch is shown in (a–c). The interaction strength is the same in (c) and (d), and the descending solid line in (d) is a piecewise addition of the solid and dashed lines in (c).

H_{SF} : Switching from \downarrow to \uparrow and from \uparrow and \downarrow occurs at $H = \pm H_{\text{SF}}$, respectively, and the corresponding hysteresis loop is rectangular. Because the particles are nonequivalent, the ensemble exhibits a *switching-field distribution* $P(H_{\text{SF}})$, and the net magnetization $M = f_o(H)$ is obtained as a straightforward superposition of the individual switching events. For example, the ascending branch of the hysteresis loop obeys

$$M(H) = -M_s + 2M_s \int_{-\infty}^H P(H_{\text{SF}}) dH_{\text{SF}} \quad (5)$$

Let us consider, for simplicity, the distribution $P(H_{\text{SF}}) = \frac{1}{2}(1 - \tanh^2((H_{\text{SF}} - H_o)/\Delta))$, which is peaked at H_o , has a width of the order of Δ , and yields $f_o(H) = \tanh((H - H_o)/\Delta)$. Figure 5a and the dashed line in Fig. 5d explain how this function translates into a hysteresis loop.

The next step is to add the interactions, replacing the field $H_i = H$ by $H_i = H + \sum_j W_{ij} M_j$, where i and j are particle indices. However, the corresponding materials equations, $M_i = f_o(H + \sum_j W_{ij} M_j)$, form a huge nonlinear and difficult-to-solve set. To simplify the calculation, we divide the particles into two categories or sublattices A and B, similar to the \uparrow and \downarrow columns in the lower part of Fig. 4 but not necessarily with antiparallel magnetizations M_A and M_B . This yields the materials equations

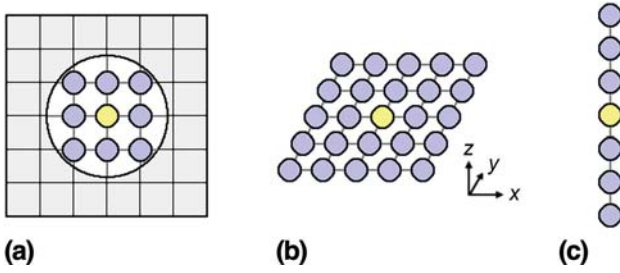


Fig. 6. Interactions and geometry: (a) side view of a bulk magnet, as described in the main text, (b) square thin-film array, and (c) particle chain. In all cases, the magnetic field is in the z -direction.

$$M_A = f_0(H + W_{AA}M_A + W_{AB}M_B) \quad (6a)$$

$$M_B = f_0(H + W_{BA}M_A + W_{BB}M_B) \quad (6b)$$

The next step is to introduce interaction parameters having the dimension of a magnetic field: $J = W_{AA}/M_s = W_{BB}/M_s$ describes intrasublattice interactions, whereas $J^* = W_{AB}/M_s = W_{BA}/M_s$ describes inter-sublattice coupling.

For the columnar structure in the bottom part of Fig. 4, $J > 0$ is positive but $J^* < 0$. This creates an instability near H_c : For large positive and large negative fields, the spin structure of the two sublattices is $\uparrow\uparrow$ and $\downarrow\downarrow$, respectively, but in small fields, $\uparrow\downarrow$ or $\downarrow\uparrow$ may be preferred. Figure 5 shows the evolution of the hysteresis loops as the interaction strength is increased. In Fig. 5b and c, there are regions with three possible magnetization values, which is a consequence of the nonlinearity of Eq. 6. However, only the monotonically increasing branch is physically realized.

The instability provided by Eq. 6 can also be investigated by linearization and eigenmode analysis. This procedure is mathematically similar to the mean-field analysis of the Néel transition in antiferromagnets³⁷ but physically different. At $H = \pm H_0$,

$$M_A = \frac{1}{\Delta}(JM_A + J^*M_B) \quad (7a)$$

$$M_B = \frac{1}{\Delta}(J^*M_A + JM_B) \quad (7b)$$

These two equations yield instabilities at $J + J^* = \Delta$ (overskewing) and $J - J^* = \Delta$ (column formation). The coupling constants J and J^* depend on the spatial arrangement of the interacting particles. Let us assume that nearest neighbors are coupled by a positive exchange interaction J_0 and by magnetostatic interactions of $+J_{MS}$ (axial coordination) and $-1/2J_{MS}$ (planar coordination), corresponding to the $1/2(3\cos^2\theta - 1)$ character of dipole interactions. Figure 6 shows the geometries for which we evaluate J and J^* .

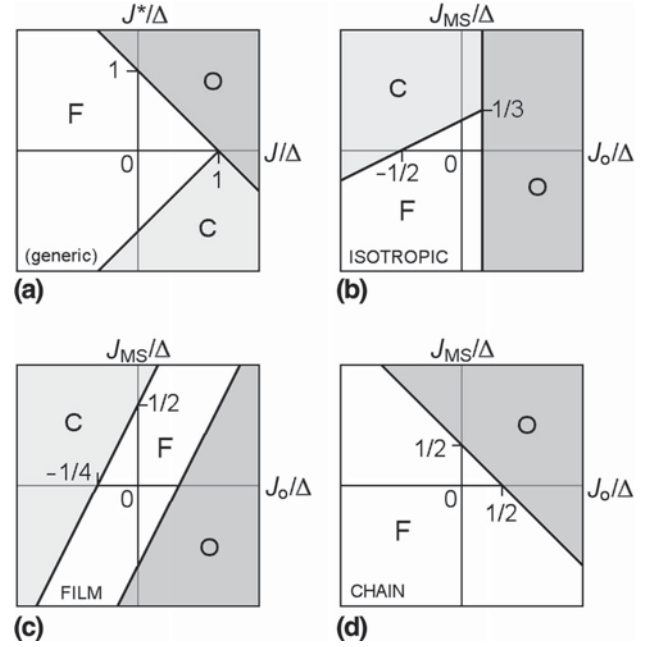


Fig. 7. Phase diagram for spin structures near coercivity: (a) Eq. 6 and (b–d) the ensembles of Fig. 6a–c. The respective capital letters F, O, and C denote behavior similar to interaction-free particles, overskewing, and the formation of columns (“interaction domains”).

In “structurally isotropic” bulk arrays (Fig. 6a), each particle has two axially coordinated nearest neighbors (top and bottom) and four nearest neighbors with planar coordination. The axial and planar neighbors belong to different sublattices, and the interaction parameters are $J = 2J_0 + 2J_{MS}$ and $J^* = 4J_0 - 2J_{MS}$. From J and J^* , we obtain the overskewing line $J_0 = 1/6$ and the columnar instability line $\Delta + 2J_0 = 4J_{MS}$. In thin films (Fig. 6b), the four nearest neighbors belong to the second sublattice, so that $J^* = 4J_0 - 2J_{MS}$, as in the bulk. However, because there are no nearest neighbors belonging to the same sublattice, $J = 0$. This yields the respective columnar-instability and overskewing lines $J_{MS} = 2J_0 \pm \Delta/2$. Finally, the particle chain exhibits $J = 2J_0 + 2J_{MS}$ and $J^* = 0$, corresponding to a line $\Delta = 2J_0 + 2J_{MS}$ that describes the onset of overskewing. Figure 7 shows the phase diagrams for Eq. 6 and for the three particle ensembles of Fig. 6.

Permanent magnets operate in the second quadrant of the hysteresis loop, and Fig. 5d shows that magnetostatic flux closure negatively affects the performance of the magnets. Physically, the net magnetization collapses, as in Fig. 3b, and it no longer creates a usable magnetic field in free space. However, magnetostatic interactions are often, but not always, harmful and may even be exploited for innovative technologies. Figure 8 shows one example, namely nanostructured MnBi:FeCo bilayers and multilayers. As we will discuss elsewhere, such thin films can be produced with the MnBi c -axis perpendicular to the film plane.

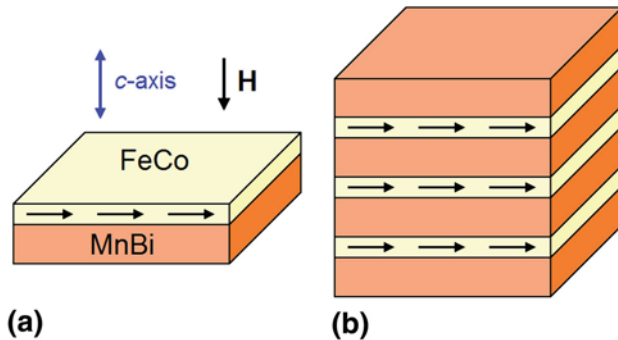


Fig. 8. Relative c -axis orientation: (a) parallel to interface, (b) perpendicular to interface, and (c) $M(H)$ loops in the first and second quadrants. The arrows show the easy axis and magnetization orientation in the hard phase.

In large magnetic fields H , the magnetization of the soft FeCo phase is parallel to the field, but on decreasing H , the FeCo magnetization rapidly starts to turn into the film plane. This is partially due to the nucleation effects described in the section titled, “Geometrical Optimization,” aggravated by the soft free surface,¹¹ and partially due to magnetostatic interactions, which favor the magnetization lying in the film plane. However, this mechanism yields positive effects where it counts, namely in the second quadrant of the hysteresis loop. Here, the in-plane magnetization of the soft phase creates a “barrier” against the rapid decrease of the magnetization as the magnetic field becomes more negative. Interestingly, and rather unusual for thin-film magnets, the effect persists if the MnBi:FeCo bilayers are mounted on top of each other, as in Fig. 8b. This is important because thin-film magnets cannot be used directly as permanent magnets.³ Note that the configuration of Fig. 8b is not the globally most stable one because the in-plane magnetizations of the soft planes may order antiferromagnetically and undergo curling. These effects are likely to further improve the performance in the second quadrant, but further research is necessary to investigate these effects.

DISCUSSION AND CONCLUSION

It is important to keep in mind that this article focuses on magnets where the hard phase is c -axis aligned, as contrasted to isotropic magnets.³⁸ The latter promises lower energy products because the hard phase does not fully contribute to the magnetization. However, isotropic two-phase nanostructures like $\text{Nd}_2\text{Fe}_{14}\text{B}$ predate the research on aligned two-phase magnets and are much easier to produce, even in an industrial context.^{39–41} Two-phase magnets with c -axis alignment are usually only partially c -axis aligned or “textured,” but such magnets are physically closer to fully aligned magnets.^{24,42} For example, in the limit of very small grain sizes, the average anisotropy $\langle K \rangle$ of isotropic magnets becomes zero,³⁸ whereas those of partially aligned

magnets remain nonzero and are typically a large fraction of K_1 .⁴²

It is instructive to discuss the micromagnetic susceptibility χ (known as α in magnetic recording) of the two-sublattice model of Eq. 6. The interaction-free susceptibility $\chi_o = dM/dH$, measured at H_c and corresponding to Fig. 5a, is equal to M_s/Δ . In the interacting case, analysis of Eqs. 6 and 7 yields

$$\chi = \frac{\chi_o}{1 - \chi_o(J + J^*)/M_s} \quad (8)$$

First, this equation confirms that the loop slope becomes infinite when $J + J^*$ approaches the width Δ of the switching-field distribution. Second, relations such as Eq. 8 are frequently encountered in interacting systems.^{43,44} They describe, on a mean-field level, how single-particle properties are modified by interactions. Well-known examples are the onset of itinerant metallic ferromagnetism, as described by the Stoner criterion,⁴³ and ferromagnetic ordering at the Curie point.⁴⁴ A common feature of all these mechanisms is the transition from a non-cooperative or “civilian” regime to a cooperative or “military” regime, where all atoms or particles are involved simultaneously.

In conclusion, we have investigated how the performance of aligned hard-soft nanocomposites depends on nanogeometry. Both coercivity and the volume fraction f of the soft phase in the hard matrix are important, and our “sandbox game” advocates soft-magnetic cubes or rods with a square cross section. Magnetostatic interactions tend to create flux-closure configurations that deteriorate the coercivity and energy product. However, magnetostatic effects can be exploited innovatively in MnBi:FeCo bilayers and multilayers because the energy product is determined in the second quadrant. Additional theoretical research is necessary to determine secondary magnetostatic effects, such as interaction between the layers in Fig. 8b and curling inside the soft layers. These effects are likely to further improve the energy product.

ACKNOWLEDGMENTS

The research is supported primarily by PNNL ARPA-E (to J.C., I.T., P.M., and R.S.) and partially by NSF MRSEC DMR-0820521 and ARO W911NF-10-2-0099 (to R.S. and P.M.).

REFERENCES

1. J.F. Herbst, *Rev. Mod. Phys.* 63, 819 (1991).
2. K. Kumar, *J. Appl. Phys.* 63, R13 (1988).
3. R. Skomski and J.M.D. Coey, *Permanent Magnetism* (Bristol: Institute of Physics, 1999).
4. D. Weller and T. McDaniel, *Advanced Magnetic Nanostructures*, ed. D.J. Sellmyer and R. Skomski (Berlin, Germany: Springer, 2006), pp. 295–32.
5. R.L. Comstock, *Introduction to Magnetism and Magnetic Recording* (New York: Wiley, 1999).
6. A. Aharoni, *Rev. Mod. Phys.* 34, 227 (1962).
7. D. Givord and M.F. Rossignol, *Rare-Earth Iron Permanent Magnets*, ed. J.M. D. Coe (Oxford, U.K.: University Press, 1996), pp. 218–285.

8. J.M.D. Coey, *IEEE Trans. Magn.* 49, 4671 (2011).
9. L.H. Lewis, A. Mubarak, E. Poirier, N. Bordeaux, P. Manchanda, A. Kashyap, R. Skomski, J. Goldstein, F.E. Pinkerton, R.K. Mishra, R.C. Kubic Jr, and K. Barmak, *J. Phys. Condens. Matter* 26, 064213 (2014).
10. P. Kumar, A. Kashyap, B. Balamurugan, J.E. Shield, D.J. Sellmyer, and R. Skomski, *J. Phys. Condens. Matter* 26, 064209 (2014).
11. R. Skomski, P. Manchanda, P. Kumar, B. Balamurugan, A. Kashyap, and D.J. Sellmyer, *IEEE Trans. Magn.* 49, 3215 (2013).
12. E.F. Kneller and R. Hawig, *IEEE Trans. Magn.* 27, 3588 (1991).
13. R. Skomski and J.M.D. Coey, *Phys. Rev. B* 48, 15812 (1993).
14. E.E. Fullerton, S.J. Jiang, and S.D. Bader, *J. Magn. Magn. Mater.* 200, 392 (1999).
15. N. Jones, *Nature* 472, 22 (2011).
16. P. Liu, C.P. Luo, Y. Liu, and D.J. Sellmyer, *Appl. Phys. Lett.* 72, 483 (1998).
17. D. Roy and P.S. Anil Kumar, *J. Appl. Phys.* 106, 073902 (2009).
18. E. Goto, N. Hayashi, T. Miyashita, and K. Nakagawa, *J. Appl. Phys.* 36, 2951 (1965).
19. H. Kronmüller, *Phys. Status Solidi B* 144, 385 (1987).
20. S. Nieber and H. Kronmüller, *Phys. Status Solidi B* 153, 367 (1989).
21. R. Skomski, *Phys. Status Solidi B* 174, K77 (1992).
22. R. Skomski and J.M.D. Coey, *IEEE Trans. Magn.* 30, 607 (1994).
23. R. Skomski, *J. Appl. Phys.* 83, 6503 (1998).
24. R. Skomski, *J. Phys. Condens. Matter* 15, R841 (2003).
25. T. Schrefl and J. Fidler, *J. Appl. Phys.* 83, 6262 (1998).
26. A. Szlaferek, *Phys. Status Solidi B* 241, 1312 (2004).
27. J.S. Jiang and S.D. Bader, *J. Phys. Condens. Matter* 26, 064214 (2014).
28. J.P. Liu, R. Skomski, Y. Liu, and D.J. Sellmyer, *J. Appl. Phys.* 87, 6740 (2000).
29. J. Lyubina, K.-H. Müller, M. Wolf, and U. Hannemann, *J. Magn. Magn. Mater.* 322, 2948 (2010).
30. W.F. Brown, *Micromagnetics* (New York: Wiley, 1963).
31. D.J. Craik and E.D. Isaak, *Proc. Phys. Soc.* 76, 160 (1960).
32. G.C. Hadjipanayis and W. Gong, *J. Appl. Phys.* 64, 5559 (1988).
33. K. Khlopkov, O. Gutfleisch, R. Schäfer, D. Hinz, K.-H. Müller, and U.L. Schultz, *J. Magn. Magn. Mater.* 272, E1937 (2004).
34. R. Skomski, J.-P. Liu, and D.J. Sellmyer, *Phys. Rev. B* 60, 7359 (1999).
35. F. Preisach, *Z. Phys.* 94, 277 (1935).
36. R. Skomski and D.J. Sellmyer, *J. Appl. Phys.* 89, 7263 (2001).
37. J.S. Smart, *Effective Field Theories of Magnetism* (Philadelphia, PA: Saunders, 1966).
38. G. Herzer, *J. Magn. Magn. Mater.* 112, 258 (1992).
39. R. Coehoorn, D.B. de Mooij, J.P.W.B. Duchateau, and K.H.J. Buschow, *J. Phys.* 49(C-8), 669 (1988).
40. J. Schneider, D. Eckert, K.-H. Müller, A. Handstein, H. Mühlbach, H. Sassik, and H.R. Kirchmayr, *Mater. Lett.* 9, 201 (1990).
41. A. Manaf, R.A. Buckley, and H.A. Davies, *J. Magn. Magn. Mater.* 128, 302 (1993).
42. R. Skomski, *J. Magn. Magn. Mater.* 157, 713 (1996).
43. P. Fulde, *Electron Correlations in Molecules and Solids* (Berlin, Germany: Springer, 1991).
44. J.M. Yeomans, *Statistical Mechanics of Phase Transitions* (Oxford, U.K.: Oxford University Press, 1992).